Simulation Modelling Practice and Theory 33 (2013) 28–44

Contents lists available at SciVerse ScienceDirect

Simulation Modelling Practice and Theory

journal homepage: www.elsevier.com/locate/simpat

Modeling and simulation results on a new Compton scattering tomography modality

Gaël Rigaud [a,*], Maï K. Nguyen [a], Alfred K. Louis [b]

[a] Laboratoire Équipes Traitement de l'Information et Systèmes, ETIS-ENSEA/University of Cergy-Pontoise/CNRS UMR 8051, 6 avenue du Ponceau, 95014 Cergy-Pontoise Cedex, France
[b] Fachbereich Mathematik, Universität des Saarlandes, D-66041 Saarbrücken, Germany

ARTICLE INFO

Article history:
Available online 11 May 2012

Keywords:
Modeling
Simulation
Algorithm
Biomedical imaging
Compton scattering tomography
Image reconstruction

ABSTRACT

Conventional tomography (X-ray scanner, Single Photon Emission Computed Tomography, Positron Emission Tomography, etc.) is widely used in numerous fields such as biomedical imaging, non-destructive industrial testing and environmental survey, etc. In these tomographies, a detector rotates in space to collect primary radiation emitted or transmitted by an object under investigation. In this case Compton scattered radiation behaves as noise hindering image quality and consequently correction to scatter should be required. However recently an interesting new imaging concept, which uses precisely scattered radiation as imaging agent, has been advocated. The camera records now images labeled by scattered photon energy or equivalently by scattering angle. In the present paper we propose a new modality of Compton scattering tomography (CST), akin to the X-ray scanning tomography, in the sense that it works in transmission modality but uses Compton scattered radiation to recover the electron density of the studied medium. The new image formation modeling is based on a new class of Radon transforms on circular arcs (CART). Through numerical simulation results we show the feasibility and the relevance of this new imaging process.

1. Introduction to Compton scattering tomography (CST) and circular-arc Radon transform

For more than fifty years, transmitted penetrating radiation such as X- or gamma-rays have been routinely used to probe the hidden parts of matter and/or tissues [1–3]. The measurement of their attenuation along all possible linear paths in a plane forms a set of Radon data, which, once fed into a chosen inversion formula, provides the reconstruction of the probed medium. In this imaging modality, scattered radiation acts as a nuisance blurring images hence it should be removed or at least be compensated.

However it was realized, in the early seventies, that the Compton effect may give rise to new challenging imaging modalities, in which the camera records images labeled by scattered photon energies. Then it is shown that the three dimensional image reconstruction from scattered radiation data is feasible [4–8].

Let us recall that the Compton effect (Fig. 1) is the scattering of X- or gamma-photons with electric charges. The energy of a scattered photon is related to the scattering angle ω by the Compton relation

$$E_\omega = \frac{E_0}{1 + \frac{E_0}{mc^2}(1 - \cos\omega)}, \tag{1}$$

* Corresponding author. Tel.: +33 0130736279.
E-mail addresses: gael.rigaud@ensea.fr (G. Rigaud), mai.nguyen-verger@u-cergy.fr (M.K. Nguyen), louis@num.uni-sb.de (A.K. Louis).

1569-190X/$ - see front matter © 2012 Elsevier B.V. All rights reserved.
http://dx.doi.org/10.1016/j.simpat.2012.03.007

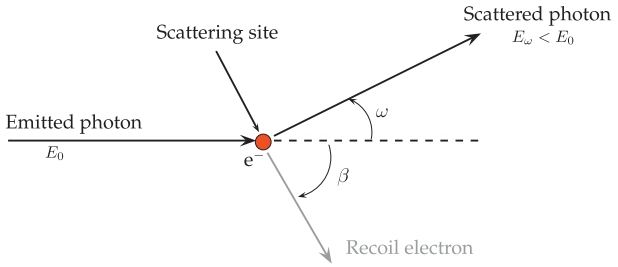

Fig. 1. Principle of Compton scattering.

where E_0 is the emitted photon energy and mc^2 represents the energy of an electron at rest (0.511 MeV).

The idea is to register the outgoing scattered photons according to their energies in order to image the hidden part of objects of interest. This is the basic idea in Compton scattering tomography (CST).

In 1994, Norton [9] worked out a CST modality which is based on a Radon transform on circles having a fixed common point. The functioning principle is given in Fig. 2. A point source **S** emits primary radiation towards an object, of which **M** is a scattering site (running point). A point detector **D** moves along an *Ox*-axis and collects, at given energy E_ω, scattered radiation from the object. The physics of Compton scattering demand that the registered radiation flux density I at position **D** is due to the contribution of all scattering sites **M** lying on an arc of circle from **S** to **D** subtending an angle $(\pi - \omega)$, where ω is the scattering angle corresponding to the outgoing energy E_ω (see Eq. (1)).

Norton gave the expression of the registered radiation flux density I as

$$I(\rho,\varphi) = (\mathcal{C}^1 f)(\rho,\varphi) = \int_0^{\pi} d\theta \int_0^{\infty} dr f(r,\theta) w(r,\theta;\rho,\varphi)\delta[r - 2\rho\cos(\theta-\varphi)],$$

where $f(r,\theta)$ stands for the object electron density and $\mathcal{C}^1$ is the operator of the Norton Radon transform, $\delta(.)$ is the 1-D Dirac delta function and $w(.)$ is defined by

$$w(r,\theta;\rho,\varphi) = \frac{a\ r\ s(\theta)P(\omega = \pi/2 + \varphi)}{4\pi\ (2\rho)^3 \sin^2\theta} = w_1(r,\theta)\cdot w_2(\rho,\varphi).$$

In the above formula, a represents the area of an element of detection, $s(\theta)$ expresses any angular dependance of the γ-ray source distribution, and $P(\omega)$ is the Klein-Nishina differential cross-section. Mathematically, $I(p,\varphi)$ is essentially the Radon transform of the object electron density $f(r,\theta)$ on arcs of circle, when radiation attenuation and photometric effects on radiation propagation are not taken into account.

Norton worked out an inversion formula

$$f(r,\theta) = \frac{1}{\pi^2}\int_0^{2\pi} d\varphi \int_0^{\infty} \rho\ d\rho \frac{(\mathcal{C}^1 f)(\rho,\varphi)}{w(r,\theta;\rho,\varphi)} h[r - 2\rho\cos(\theta-\varphi)]$$

where

$$h(x) = \int_{-\infty}^{\infty} e^{-i\zeta x}|\zeta| d\zeta. \tag{2}$$

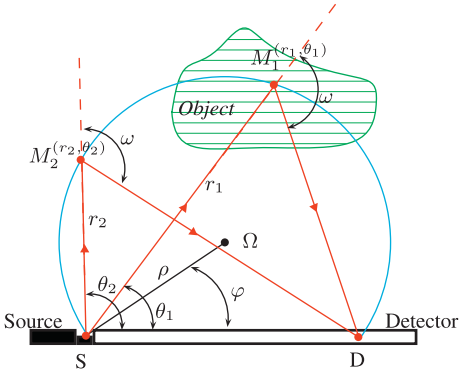

Fig. 2. Principle of Norton's CST.

This expression has the same the convolution kernel in the filtered Back-Projection algorithm used in X-ray transmission CT. The difference is that the Back-Projection is performed along straight lines in transmission CT, whereas here the Back-Projection is performed along the circles of equation $r = 2\rho\cos(\theta - \varphi)$.

However $h(x)$ in Eq. (2) should be interpreted as a distribution, since the ζ-integral does not converge. This is why Norton proposed an "apodization" function $A(\zeta)$ which goes to zero smoothly beyond a spatial-frequency cutoff (indeed the function $f(r,\theta)$ is assumed to be bandlimited) and placed it under the integral.

Recently we have suggested a novel modality for Compton scattering tomography [10]. The physical principle is similar to Norton's CST, however in our configuration the source is not fixed but rotates around the object in order to collect more scattered photons. In this paper we prove that the corresponding Radon transform is invertible by Back-Projection and describe in more details the simulation process than in [10].

Section 2 shows how image formation process in the new CST is modeled and how the collected data leads to a Radon transform on a particular class of circular arcs, which is called Circular-Arc Radon transform (CART).

Section 3 summarizes the inversion procedure of the CART which takes its origin from a relation between the CART and the ordinary Radon transform (RT).

In Section 4 we present numerical simulations on image formation and reconstruction for a Shepp-Logan phantom and a nuclear waste phantom to support the feasibility of the new CST. The paper ends with a short conclusion on the obtained results and opens some future research perspectives.

2. Modeling of the new modality in Compton scattering tomography (CST)

2.1. Forward circular-arc Radon transform (CART) and associated Compton scattering tomography

Consider a 2D-object represented by its electron density, a non-negative continuous function $f(r,\theta)$ with bounded support. An emitting radiation point source **S** is placed at a distance $2p$ from a point detector **D**. It is important for the inversion procedure to consider only the upper part of the object, this is why an angle collimator is placed at **D**. The segment **SD** rotates around its middle **O** and its angular position is given by φ, see Fig. 3.

The source **S** irradiates the studied medium and according to Compton effect, emitted photons are scattered by interaction with electric charges (see Eq. (1)). As the detector **D** can monitor scattered photons according to scattered energies, some of these scattered photons are collected by the detector at their corresponding energies E_ω. Thus, for a fixed φ, to each energy E_ω corresponds a set of scattering sites on a circular-arc $C(\varphi,\omega)$.

Finally the detected radiation flux density $g(\varphi,\omega)$ is proportional to the integral of the electron density $f(\mathrm{M})$ with $\mathrm{M} \in C(\varphi,\omega)$. It can be written as

$$g(\varphi,\omega) = \int_{(r,\theta)\in C(\varphi,\omega)} w(r,\theta;\varphi,\omega) f(r,\theta) ds \tag{3}$$

where ds is the elementary length of circular-arc to be computed from the circular arc equation

$$r = p(\sqrt{1+\tau^2\cos^2\gamma} - \tau\cos\gamma), \tag{4}$$

where $\tau = \cot\omega$ and $\gamma = \theta - \varphi$, with $(\varphi,\omega) \in [0,2\pi] \times]0,\frac{\pi}{2}[$. In Eq. (3), the weighting function $w(r,\theta;\varphi,\omega)$ incorporates physical effects: angular dependance of the Compton scattering and radiation divergence and is given by

$$w(r,\theta;\varphi,\omega) = \frac{b\ P(\omega)}{(1+\tan^2\omega)\cdot(p^2-r^2)^2} = w_1(r)\cdot w_2(\omega),$$

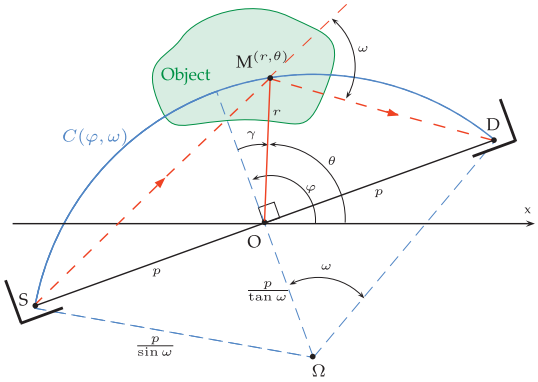

Fig. 3. Principle of the new CST based on the CAR transform.

where b is a constant, $P(\omega)$ is the Klein-Nishina probability and the factor represents the product of traveling square distances of a detected photon

$$SM^2 \cdot MD^2 = (1+\tan^2\omega)\cdot(p^2-r^2)^2.$$

Due to the form of the weighting function w which can be separated in two functions $w_1(r)$ and $w_2(\omega)$ and hence does not change the inversion procedure, we restrict our forward transform to the integral of a function f over correspondings circular arcs. Thus $g(\varphi,\omega)$ appears as the Radon transform on arcs of circles of $f(r,\theta)$, i.e. the CART $(\mathcal{C}^2 f)(\varphi,\tau)$ given by

$$g(\varphi,\omega) = (\mathcal{C}^2 f)(\varphi,\tau) = \int_{-\frac{\pi}{2}}^{\frac{\pi}{2}} f(r(\gamma),\gamma+\varphi)r(\gamma)\frac{\sqrt{1+\tau^2}}{\sqrt{1+\tau^2\ \cos^2(\gamma)}}d\gamma. \tag{5}$$

Eq. (5) describes image formation.

2.2. Modeling of image formation process

For fixed (φ,ω), we calculate the set of points (r,θ) on the circular-arc $C(\varphi,\omega)$ (Eq. (4)). Then to get $g(\varphi,\omega)$ (or projections), we multiply $f(r,\theta)$ by a differential element (Eq. (5)) and sum over pixels along the circular arc $C(\varphi,\omega)$. Fig. 4 shows how we scan the object to simulate measurements.

For small values of $\omega(\omega\approx 0)$, the scanning of the circular-arc becomes hard. According to the sampling rate $d\theta$, we can define an angle ω_0, below which we cannot get all the points of the circular-arc. This is why the area under the circular-arc $C(\varphi,\omega_0)$ is "ill-observed" hence "ill-reconstructed". Numerically we can reduce this phenomenon by decreasing $d\theta$ but at the expense of the computational time.

To avoid it, we have to rewrite the image formation. Now we study a new function $h(x,y)$ which is $f(r,\theta)$ in cartesian coordinates and we consider the rotating basis centered at Ω. The scanning of the corresponding circular-arc $C(\varphi,\omega)$ is now parametrized by $\alpha\in[\pi/2-\omega,\pi/2+\omega]$, see Fig. 5.

In the fixed basis centered at O a point M(x,y) of $C(\varphi,\omega)$ can be defined by α according to the following system

$$\begin{cases} x(\alpha) = \frac{p}{\sin\omega}\sin(\alpha+\varphi) - \frac{p}{\tan\omega}\cos\varphi \\ y(\alpha) = \frac{-p}{\sin\omega}\cos(\alpha+\varphi) - \frac{p}{\tan\omega}\sin\varphi. \end{cases}$$

Considering these variables, the integral of a function $f(r,\theta)$ on circular-arcs becomes the integral of the corresponding cartesian function $h(x,y)$ on corresponding circular sector

$$(\mathcal{C}^2 f)(\varphi,\tau) = \int_{-\frac{\pi}{2}}^{\frac{\pi}{2}} f(r(\gamma),\gamma+\varphi)r(\gamma)\frac{\sqrt{1+\tau^2}}{\sqrt{1+\tau^2\ \cos^2(\gamma)}}d\gamma = \int_{\frac{\pi}{2}-\omega}^{\frac{\pi}{2}+\omega} p\sqrt{1+\tau^2}h(x(\alpha),y(\alpha))d\alpha. \tag{6}$$

Eq. (6) is not suitable for inversion but is more adapted to a computation of the image formation.

2.3. Integral kernel and point spread function (PSF)

Alternatively Eq. (5) can be put under the form of an integral transform in $\left[\varphi-\frac{\pi}{2},\varphi+\frac{\pi}{2}\right]\times\mathbb{R}^+$ with a delta function kernel concentrated on the arc of circle $C(\varphi,\omega)$

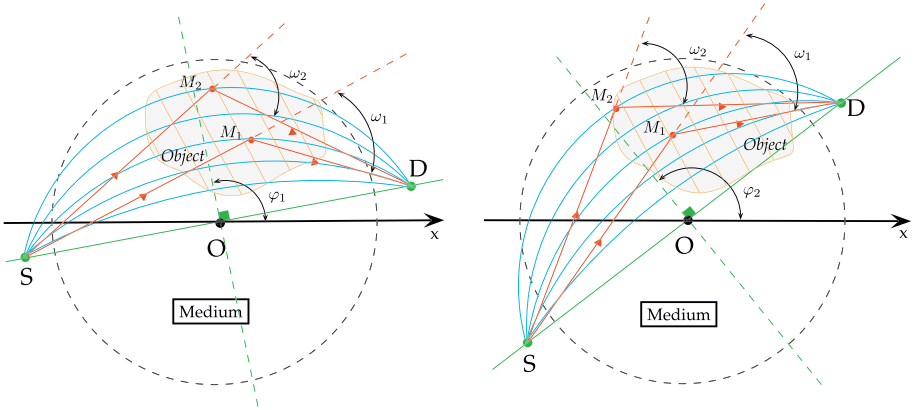

Fig. 4. Scanning of the medium.

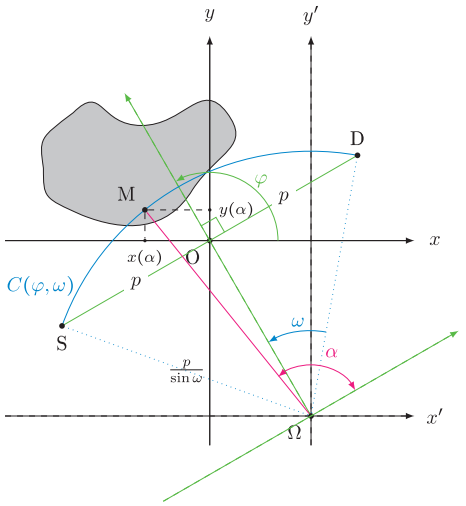

Fig. 5. Principle of CART in cartesian coordinates.

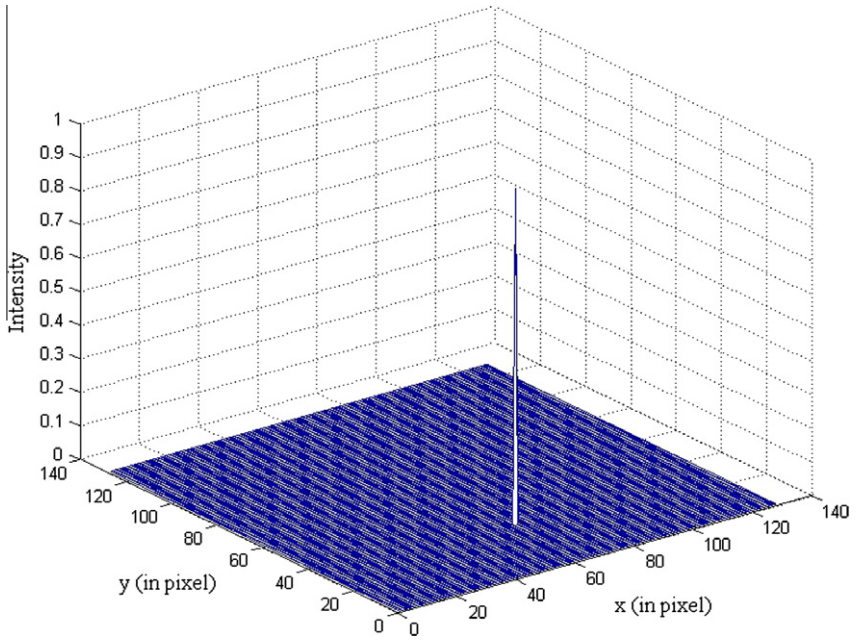

Fig. 6. 3D representation of a point object.

$$\mathcal{C}^2 f(\varphi,\tau) = \int_{\varphi-\frac{\pi}{2}}^{\varphi+\frac{\pi}{2}} \int_0^{\infty} f(r,\theta)\mathcal{K}_{\mathcal{C}^2}(\varphi,\tau|r,\theta) r dr d\theta \tag{7}$$

with

$$\mathcal{K}_{\mathcal{C}^2}(\varphi,\tau|r,\theta) = \frac{\sqrt{1+\tau^2}}{\sqrt{1+\tau^2\cos^2(\theta-\varphi)}}\delta(r - p(\sqrt{1+\tau^2\cos^2(\theta-\varphi)} - \tau\cos(\theta-\varphi))). \tag{8}$$

For a single point object (Fig. 6), located at (r_0,θ_0), represented by

$$f_0(r,\theta) = \frac{1}{r}\delta(r-r_0)\delta(\theta-\theta_0),$$

the response of the CART (Eq. (7)), called the point spread function (PSF), is given by the equation

$$(\mathcal{C}^2 f_0)(\varphi,\tau) = \frac{\sqrt{1+\tau^2}}{\sqrt{1+\tau^2\cos^2(\theta_0-\varphi)}}\delta(r_0 - p(\sqrt{1+\tau^2\cos^2(\theta_0-\varphi)} - \tau\cos(\theta_0-\varphi))).$$

Rewriting the kernel in terms of a τ-integration by transforming the delta-function, the PSF takes the following form

$$(\mathcal{C}^2 f_0)(\varphi,\tau) = \frac{\sqrt{1+\tau^2}}{p\cos(\theta_0-\varphi)(\sqrt{1+\tau^2\cos^2(\theta_0-\varphi)} - \tau\cos(\theta_0-\varphi))}\delta\left(\tau - \frac{p^2-r_0^2}{2pr_0\cos(\theta_0-\varphi)}\right).$$

So the support of the PSF is the curve $\omega(\varphi)$ defined by

$$\omega = \arctan\left(\frac{2pr_0}{p^2-r_0^2}\cos(\theta_0-\varphi)\right).$$

Fig. 7 shows the shape of the arctan function which characterizes the PSF support. In future works, we could study others mathematical properties of the circular-arc Radon transform such as its null space or its relation to orthogonal functions [11].

3. The inverse transform of the circular-arc Radon transform

The inverse transform can be worked out using the A.M. Cormack's technique [12] using Fourier angular components of f and of $\mathcal{C}^2 f$

$$\begin{cases} f(r,\theta) = \sum_l f_l(r)e^{il\theta} \\ \text{with} \\ f_l(r) = \frac{1}{2\pi}\int_0^{2\pi} f(r,\theta)e^{-il\theta}d\theta \end{cases} \text{and} \begin{cases} (\mathcal{C}^2 f)(\varphi,\tau) = \sum_l (\mathcal{C}^2 f)_l(\tau)e^{il\varphi} \\ \text{with} \\ (\mathcal{C}^2 f)_l(\tau) = \frac{1}{2\pi}\int_0^{2\pi}(\mathcal{C}^2 f)(\varphi,\tau)e^{-il\varphi}d\varphi. \end{cases}$$

Eq. (5) now takes the form

$$(\mathcal{C}^2 f)_l(\tau) = 2\int_0^{\frac{\pi}{2}} r(\gamma)\frac{\sqrt{1+\tau^2}}{\sqrt{1+\tau^2\cos^2(\gamma)}}f_l(\gamma)\cos(l\gamma)d\gamma.$$

The inverse formula is given in [13],

$$f_l(r) = (-)\frac{2p(p^2+r^2)}{\pi(p^2-r^2)^2}\left[\frac{d}{dt}\int_t^\infty \frac{\cosh\left(l\cosh^{-1}\left(\frac{q}{t}\right)\right)}{q\sqrt{\left(\frac{q}{t}\right)^2-1}}\frac{(\mathcal{C}^2 f)_l\left(\frac{1}{q}\right)}{\sqrt{1+q^2}}dq\right]_{t=\frac{2pr}{p^2-r^2}}, \tag{9}$$

where $q = 1/\tau$. Finally $f(r,\theta)$ is reconstructed through its Fourier expansion with the circular components $f_l(r)$.

In principle, one can use Eq. (9) to perform numerical computations. However Eq. (9) is numerically unstable. Assuming that the original function is bounded, a close inspection of the integral kernel of Eq. (9) shows that it behaves as

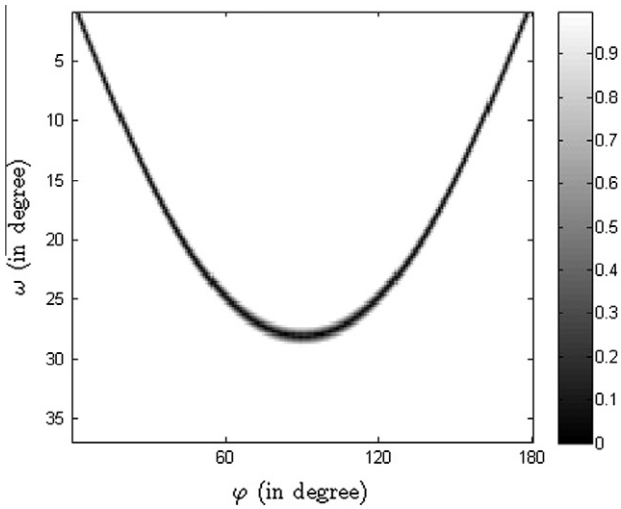

Fig. 7. CAR transform of a point object (PSF) in Fig. 6.

$$\lim_{q\to+\infty}\frac{\cosh\left(|l|\cosh^{-1}\left(\frac{q}{t}\right)\right)}{q\sqrt{\left(\frac{q}{t}\right)^2-1}}\approx\lim_{u\to+\infty}2\ e^{(|l|-2)u}, \tag{10}$$

where $u=\cosh^{-1}\left(\frac{q}{t}\right)$. Eq. (10) presents an apparent divergence when $|l|>2$, since for $q\to\infty$ the integrand grows very rapidly. The presence of noise in the data $(\mathcal{C}^2f)_l(1/q)$ for large q is badly propagated into the calculation of $f_l(r)$ which prevents simulation studies. Thus Eq. (9) needs to be regularized.

By introducing

$$\begin{cases}\check{f}_l\left(t=\frac{2pr}{p^2-r^2}\right)=\frac{(p^2-r^2)^2}{2p(p^2+r^2)}\times f_l(r)\\ \check{g}_l(q)=\frac{(\mathcal{C}^2f)_l\left(\frac{1}{q}\right)}{\sqrt{1+q^2}}.\end{cases}$$

we obtain

$$\check{f}_l(t)=(-)\frac{1}{\pi}\int_t^\infty dq\ \frac{\cosh(|l|\cosh^{-1}(q/t))}{\sqrt{q^2-t^2}}\left.\frac{d\check{g}_l(q)}{dq}\right|_{t=\frac{2pr}{p^2-r^2}}. \tag{11}$$

Eq. (11) is precisely the inverse formula of the standard Radon transform in terms of circular harmonic components. So the Radon's problem in the case of the CART could be solved by going to another space in which functions f and $\mathcal{C}^2f$ becomes the associated functions $\check{f}$ and $\check{g}$ in the standard Radon's space. Therefore another way to obtain image reconstruction based on "Filtered Back-Projection" can be proposed.

To make the ramp filter appear in the inversion formula, we proceed as follows. First we rewrite Eq. (11) as

$$\check{f}(t,\theta)=\frac{1}{2\pi^2}\int_0^\pi d\varphi\ \ \text{p.v.}\left\{\int_{-\infty}^\infty dq\frac{\partial\check{g}(\varphi,q)}{\partial q}\times\frac{1}{q-t\cos(\theta-\varphi)}\right\},$$

Next we have

$$\frac{\partial\check{g}(\varphi,q)}{\partial q}=-\int_{-\infty}^\infty du\ \delta'(q-u)\check{g}(\varphi,u),$$

so that

$$\check{f}(t,\theta)=\int_0^\pi d\varphi\int_{-\infty}^\infty du\check{g}(u,\varphi)\int_{-\infty}^\infty dq\frac{1}{2\pi^2}\frac{1}{q-t\cos(\theta-\varphi)}\delta'(q-u). \tag{12}$$

Now then set $s=(q-u)$, the q-integral in Eq. (12) is in fact the convolution product

$$\int_{-\infty}^\infty dq\frac{1}{2\pi^2}\frac{1}{q-t\cos(\theta-\varphi)}\delta'(q-u)=\int_{-\infty}^\infty ds\delta'(s)\frac{1}{2\pi^2}\frac{1}{s-(t\cos(\theta-\varphi)-u)}=\left(\delta'(s)\bigstar\frac{1}{2\pi^2}\frac{1}{s}\right)_{s=(t\cos(\theta-\varphi)-u)}.$$

Since the Fourier transforms of $\delta'(s)$ (resp. of $\frac{1}{2\pi^2}\frac{1}{s}$) is $2i\pi v$ (resp. $-i\pi\ \text{sgn}\ v$), (their product being consequently $2\pi^2|v|$), the convolution product has the Fourier representation

$$\left(\delta'(s)\bigstar\frac{1}{2\pi^2}\frac{1}{s}\right)_{s=(t\cos(\theta-\varphi)-u)}=\int_{-\infty}^\infty dv|v|e^{2i\pi v(t\cos(\theta-\varphi)-u)}.$$

Hence the inversion formula will take the form

$$\check{f}(t,\theta)=\int_0^\pi d\varphi\int_{-\infty}^\infty dv|v|e^{2i\pi v(t\cos(\theta-\varphi))}\int_{-\infty}^\infty du\check{g}(\varphi,u)e^{-2i\pi vu}.$$

This formula is just the summation image of the filtered (ramp filter) of the Back-Projected Radon data in (q,φ)-space.

Moreover we have a link between the function defined in the standard Radon transform space and the original function f defined in the original space

$$f(r,\theta)=\frac{2p(p^2+r^2)}{(p^2-r^2)^2}\check{f}\left(\frac{2pr}{p^2-r^2},\theta\right),$$

as well as

$$\check{g}(\varphi,u)=\frac{(\mathcal{C}^2f)(\varphi,1/u)}{\sqrt{1+u^2}},$$

we can write down the final inversion formula

$$f(r,\theta) = \frac{2p(p^2+r^2)}{(p^2-r^2)^2}\int_0^{\pi} d\varphi \int_{-\infty}^{\infty} dv|v| e^{2i\pi v\left(\frac{2pr}{p^2-r^2}\cos(\theta-\varphi)\right)} \int_{-\infty}^{\infty} du \frac{(\mathcal{C}^2 f)(\varphi,1/u)}{\sqrt{1+u^2}} e^{-2i\pi vu}$$
$$= \frac{2p(p^2+r^2)}{(p^2-r^2)^2}\int_0^{\pi} d\varphi \breve{g}^*\left(\varphi, \frac{2pr}{p^2-r^2}\cos(\theta-\varphi)\right).$$

This approach has the advantage to be easily implementable with short computing time. It is illustrated in Fig. 8.

4. Numerical analysis and simulation results

4.1. Numerical computation for the forward circular-arc Radon transform

Eq. (5) describes the image formation process but we have seen an alternative formulation, Eq. (6), which is more suited to a numerical computation since it considers the cartesian representation of the studied function f, h. In order to simplify the calculation of the forward CART, we use the parameter ω and the cartesian representation. From now on we consider the following notation for the image formation process

$$(\mathcal{C}^2 h)(\varphi,\omega) = \int_{\frac{\pi}{2}-\omega}^{\frac{\pi}{2}+\omega} \frac{p}{\sin\omega} h(x(\alpha),y(\alpha))d\alpha. \tag{13}$$

Let:

- H: be the original matrix of size $N \times N$ (the studied function $h(x,y)$).
- $\bar{\omega}$: be a linearly spaced vector of size N_ω from $d\omega$ to $\omega_{\max}$ where

$$\omega_{\max} = \arctan\left(\frac{\sqrt{2}pN}{p^2-\frac{N^2}{2}}\right)$$

represents the maximum value of the angle ω considering a scattering medium of size $N \times N$ and $d\omega = \frac{\omega_{\max}}{N_\omega}$ stands for the sampling step,

- $\bar{\varphi}$: be a linearly spaced vector of size N_φ from $d\varphi$ to 2π where $d\varphi = \frac{2\pi}{N_\varphi}$ is the sampling step,
- P: be the projection matrix of size $N_\varphi \times N_\omega$ corresponding to the forward CART of the cartesian function $h(x,y)$,
- $\bar{\alpha}_j$: be a linearly spaced vector of size N_α from $(\frac{\pi}{2}-\omega_j)$ to $(\frac{\pi}{2}+\omega_j)$ defined for each value of $\omega_j \in \bar{\omega}$ with a sampling step $d\alpha = \frac{2\omega_j}{N_\alpha}$,
- the following parametric system be:

$$\forall(\varphi_i,\omega_j,\alpha_k) \in \bar{\varphi}\times\bar{\omega}\times\bar{\alpha}_j, \begin{cases} x_{ijk} = \frac{p}{\sin\omega_j}\sin(\alpha_k+\varphi_i) - \frac{p}{\tan\omega_j}\cos\varphi_i \\ y_{ijk} = \frac{-p}{\sin\omega_j}\cos(\alpha_k+\varphi_i) - \frac{p}{\tan\omega_j}\sin\varphi_i. \end{cases}$$

To calculate the numerical value of this integral, we use the trapezoidal rule to interpolate H_{ijk} from $h(x_{ijk},y_{ijk})$ and we obtain the following sum

$$P_{ij} = \frac{2p}{N_\alpha}\frac{\omega_j}{\sin\omega_j}\sum_{k=1}^{N_\alpha} H_{ijk}.$$

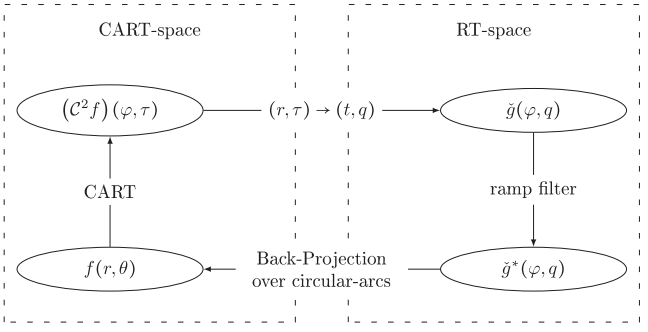

Fig. 8. Reconstruction algorithm based on "Filtered Back-Projection" over circular-arcs.

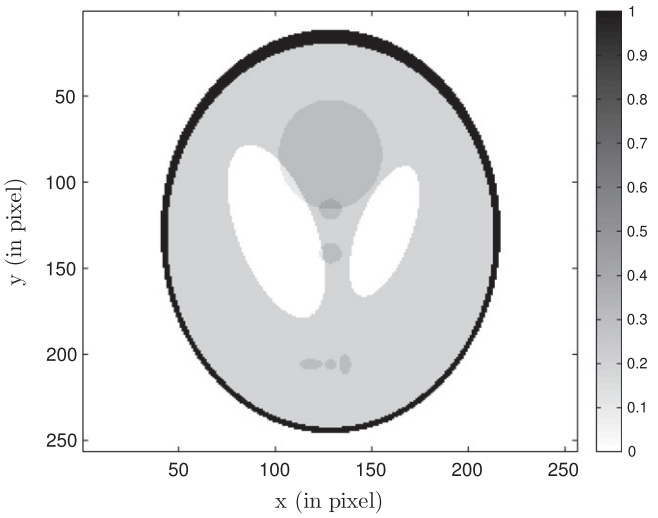

Fig. 9. Original Shepp-Logan medical phantom.

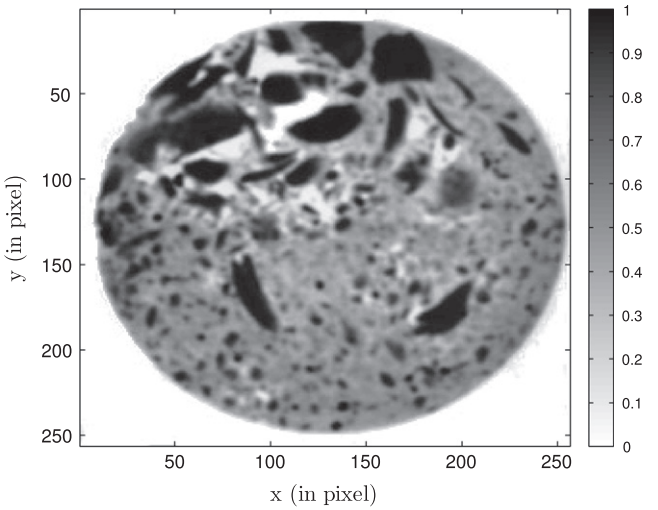

Fig. 10. Original nuclear waste phantom.

4.2. Numerical computation for the image reconstruction

Before reconstructing the original image, $h(x,y)$, we have to compute the filtering of the projections. The analytical inversion formula gives

$$h(x,y) = \frac{2p(p^2+(x^2+y^2))}{(p^2-(x^2+y^2))^2}\int_0^{\pi} \breve{g}^*\left(\varphi, \frac{2p}{p^2-(x^2+y^2)}(x\cos\varphi + y\sin\varphi)\right)d\varphi.$$

The function $\breve{g}^*(\varphi,q)$ corresponds to the filtering of the function $\breve{g}(\varphi,q) = \frac{(\mathcal{C}^2 h)(\varphi,\arctan q)}{\sqrt{1+q^2}}$. This last function is the same as in the classical Radon transform, that is to say

$$\breve{g}^*(\varphi,q) = \mathcal{F}^{-1}\{|v|\cdot\mathcal{F}\{\breve{g}(\varphi,q)\}\},$$

where $\mathcal{F}$ (resp. $\mathcal{F}^{-1}$) stands for the 1D-Fourier transform (resp. the inverse 1D-Fourier transform). Its computation is performed by a Fast Fourier transform (FFT). Because of frequency unstability and cut-off we have to apodize the ramp filter, $|v|$, with a smooth function. We choose the Hann filter defined by:

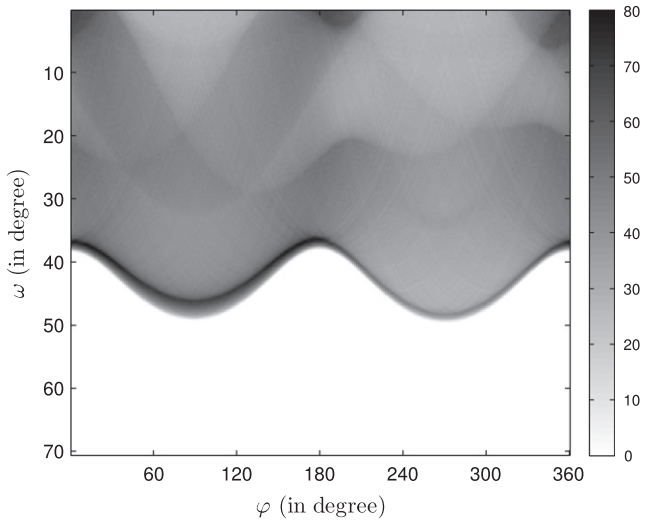

Fig. 11. CART of the medical phantom shown in Fig. 9.

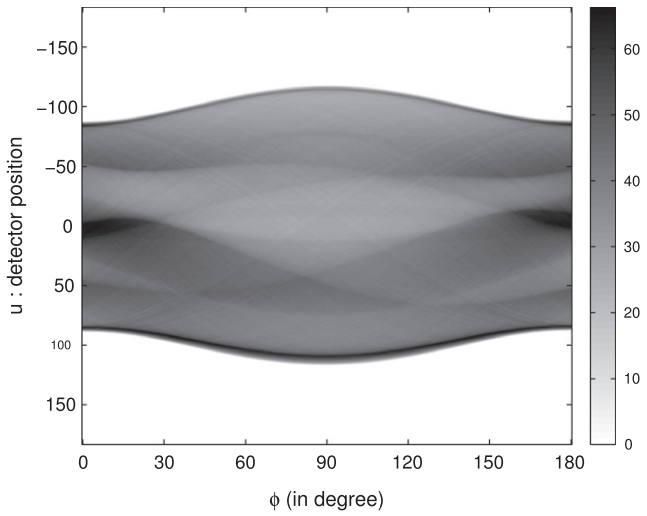

Fig. 12. Radon transform of the medical phantom shown in Fig. 9.

$$\mathcal{H}(v) = \begin{cases} 0.5\left(1+\cos\left(\pi\frac{v}{v_{\max}}\right)\right) & \text{if} \quad |v| < v_{\max} \\ 0 & \text{if} \quad |v| \geqslant v_{\max}, \end{cases}$$

where $v_{\max}$ is the maximum value of the frequency of the discretized projections. Thus the ramp filter becomes $\mathcal{H}(v)|v|$.

Then Back-Projection is applied on the curve

$$q = \frac{2p}{p^2 - (x^2+y^2)}(x\cos\varphi + y\sin\varphi),$$

which is the arc of circle $C(\varphi,\omega)$. Therefore the Back-Projection is performed over the same circular arcs as in the forward transform.

Let

- $\bar{q}$: be a linearly spaced vector of size N_q from tan$d\omega$ to tan$\omega_{\max}$ and
- G: be the filtered projections matrix of size $N_\varphi \times N_q$.

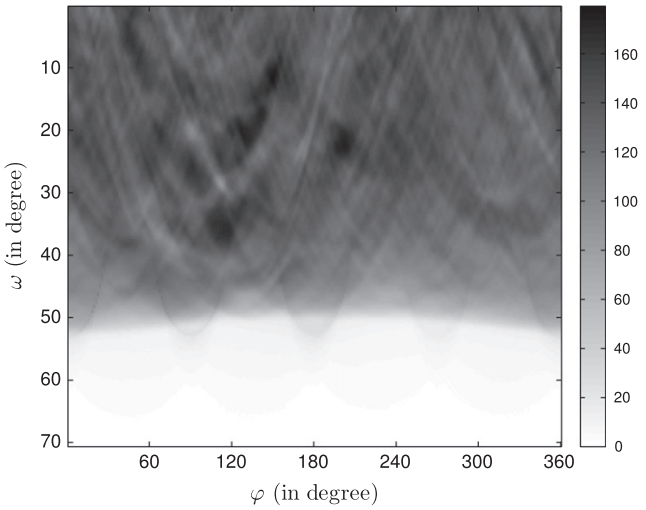

Fig. 13. CART of the nuclear waste phantom shown in Fig. 10.

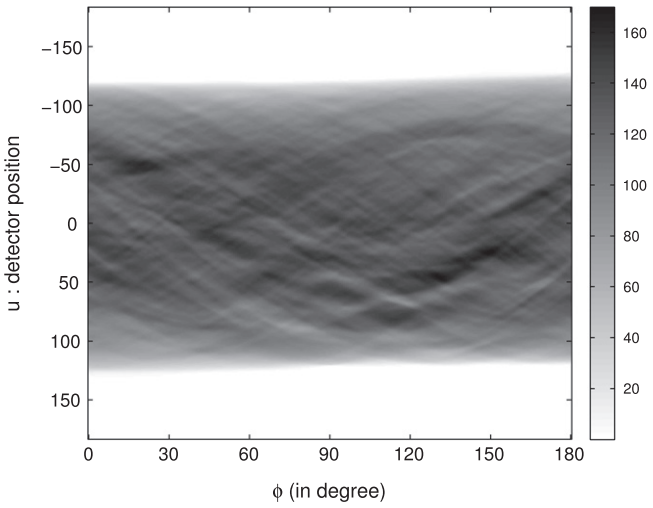

Fig. 14. Radon transform of the nuclear waste phantom shown in Fig. 10.

Therefore the Back-Projection corresponds to

$$\forall (i,j) \in [1,N]^2, \qquad H_{ij} = \frac{4\pi}{N_\varphi} \frac{p\left(p^2 + \left(x_i^2 + y_j^2\right)\right)}{\left(p^2 - \left(x_i^2 + y_j^2\right)\right)^2} \sum_{k=1}^{N_\varphi} G_{ijk},$$

where G_{ijk} is calculated by linear interpolation of $\check{g}^* \left(\varphi_k, \frac{2p}{p^2 - \left(x_i^2 + y_j^2\right)} \left(x_i \cos\varphi_k + y_j \sin\varphi_k\right) \right)$ on the vector $\bar{q}$.

4.3. Simulation results

In this section, we present the simulation results of our novel reconstruction algorithm based on the "Filtered Back-Projection" over circular-arcs in the case of the CART and compare them to the reconstruction obtained by the Radon transform Filtered Back-Projection (RT FBP).

As an illustration of the feasibility of the new CST, we carried out numerical simulations on formation and on image reconstruction for two original objects: a Shepp-Logan medical phantom (Fig. 9) and a nuclear waste phantom (Fig. 10). In order to have a "well-conditioned" problem, the number of projections ($N_\varphi \times N_\omega$) must be larger than the number of studied points ($N \times N$ here). We take $N_\varphi = N_\omega = p = N = 256$.

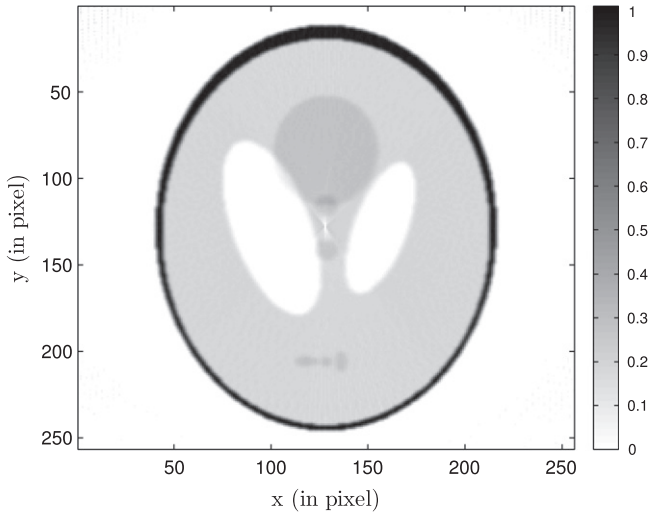

Fig. 15. Reconstruction of the medical phantom shown in Fig. 9 using CART-FBP and data in Fig. 11.

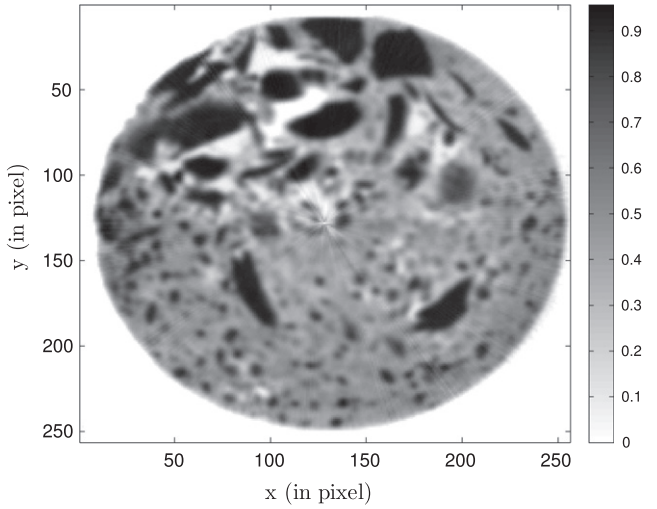

Fig. 16. Reconstruction of the nuclear waste phantom shown in Fig. 10 using CART-FBP and data in Fig. 13.

To compare the quality of the reconstructions, we define the Normalized Mean Squared Error (NMSE) and the Normalized Mean Absolute Error(NMAE)

$$NMSE = \frac{1}{N^2}\frac{\sum_{(i,j)\in[1,N]^2}|\mathcal{I}_r(i,j)-\mathcal{I}_o(i,j)|^2}{\max_{(i,j)\in[1,N]^2}\{\mathcal{I}_o(i,j)\}^2} \quad \text{and} \quad NMAE = \frac{1}{N^2}\frac{\sum_{(i,j)\in[1,N]^2}|\mathcal{I}_r(i,j)-\mathcal{I}_o(i,j)\|}{\max_{(i,j)\in[1,N]^2}\{\mathcal{I}_o(i,j)\}},$$

where $\mathcal{I}_r$ is the reconstructed image and $\mathcal{I}_o$ is the original image.

Figs. 11 and 12 (resp. Figs. 13 and 14) show the CART2 and the forward Radon transform of the Shepp-Logan phantom (resp. of the nuclear waste phantom). The CART-FBP approach gives in general a reasonable image quality in the reconstruction of the medical phantom (Fig. 15) and of the nuclear waste phantom (Fig. 16): contours and small structures are well recovered. The numerical error measurements obtained using the CART-FBP are very close to those of the ordinary Radon transform (Figs. 17 and 18), see Tab. 1. Nevertheless our reconstructions show a lot of artifacts at the corners. This is due to the non-homogeneous distribution of the intersections between circular-arcs, see Fig. 19a, this is why we have less information about the areas near the souce and the detector. This is not the case for the straigth lines which have a homogeneous distribution of the intersections, see Fig. 19b. This puts forward a sampling issue in the case of the CART. Even if the artifacts does not hinder the quality of the reconstruction, a better sampling could be studied in order to decrease the artifacts.

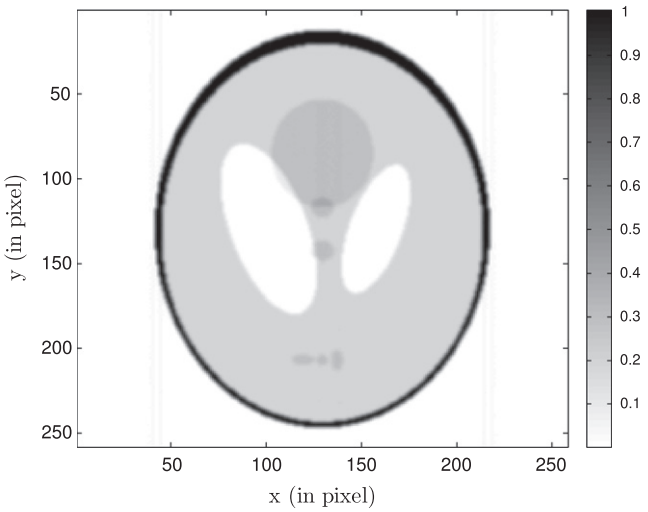

Fig. 17. Reconstruction of the medical phantom shown in Fig. 9 using RT-FBP and data in Fig. 12.

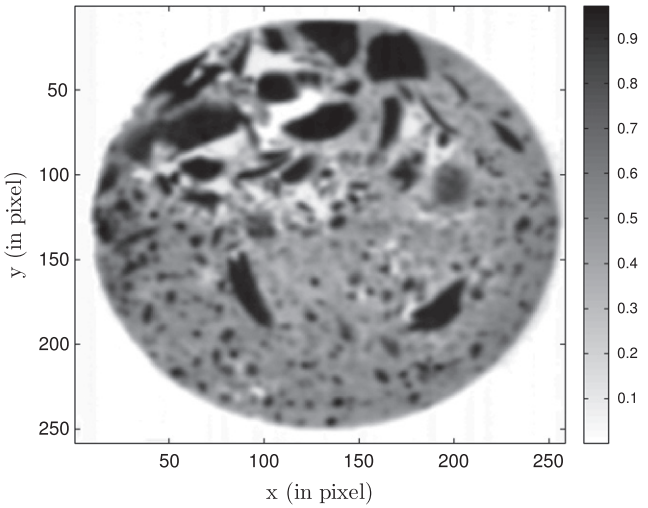

Fig. 18. Reconstruction of the nuclear waste phantom shown in Fig. 10 using RT-FBP and data in Fig. 14.

These results prove the feasibility and the interest of our algorithm in the field of medical imaging and of non-destructive testing (see Table 1).

5. Model validation using Monte-Carlo simulation

Under realistic working conditions, traveling radiation is affected by medium attenuation and by dispersion due to photometric propagation effects. In this case, these effects can be taken into account considering the following factor

$$\frac{e^{-\int_{\mathbf{MS}}\mu(x,y)dl}}{\mathbf{MS}}\times\frac{e^{-\int_{\mathbf{MD}}\mu(x,y)dl}}{\mathbf{MD}} \tag{14}$$

where $\mu(x,y)$ is the attenuation map of the studied medium. So far we have not included this factor because its presence makes the inversion of the corresponding Radon transform impossible. Moreover the Compton effect is modeled by the differential cross-section given by Klein and Nishina,

$$P(\omega)=\frac{r_e^2}{2}\frac{1}{1+\epsilon(1-\cos\omega)^2}\left(1+\cos^2\omega+\frac{\epsilon^2(1-\cos\omega)^2}{1+\epsilon(1-\cos\omega)}\right)\ \text{with}\ \epsilon=\frac{E_0}{mc^2},$$

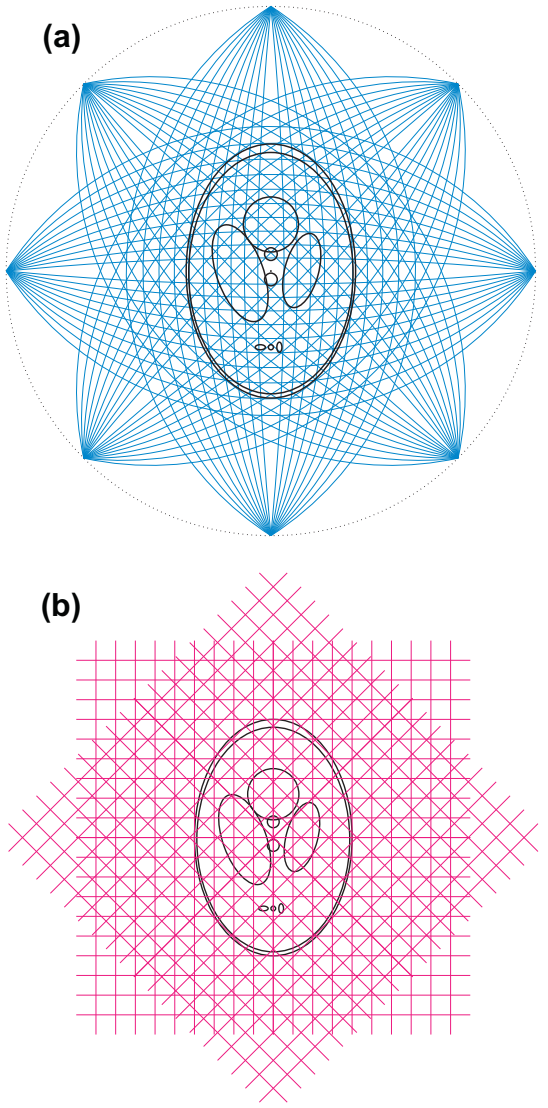

Fig. 19. Distribution of the intersections for the CART (a) and for the ordinary RT (b).

Table 1
NMSE and NMAE of different reconstructions of the Shepp-Logan phantom (Fig. 9) and of the nuclear waste (Fig. 10).

			NMAE (%)	NMSE (%)
Shepp-logan	RT-FBP	Fig. 17	1.9	0.03
	CART-FBP	Fig. 15	1.85	0.027
Nuclear waste	RT-FBP	Fig. 18	2	0.07
	CART-FBP	Fig. 16	2.5	0.05

where r_e stands for the classical radius of an electron. Using the expression

$$\mathbf{MS}\cdot\mathbf{MD} = (p^2 - r^2)\cdot\sqrt{1+\tau^{-2}}, \tag{15}$$

an exponential Circular-Arc Radon transform can be defined as:

$$\mathcal{C}^{\phi} n_e(\varphi,\tau) = \frac{p_x\, I_0\, P(\tan^{-1}(\frac{1}{\tau}))}{4\pi}\int_{-\pi/2}^{\pi/2}\tau^2\,\frac{e^{-\int_{\mathbf{MS}}\mu(x,y)dl-\int_{\mathbf{MD}}\mu(x,y)dl}}{p^2-r(\gamma)^2}\,\frac{r(\gamma)n_e(r(\gamma),\gamma-\varphi)}{\sqrt{1+\tau^2\cos^2(\gamma)}}d\gamma, \tag{16}$$

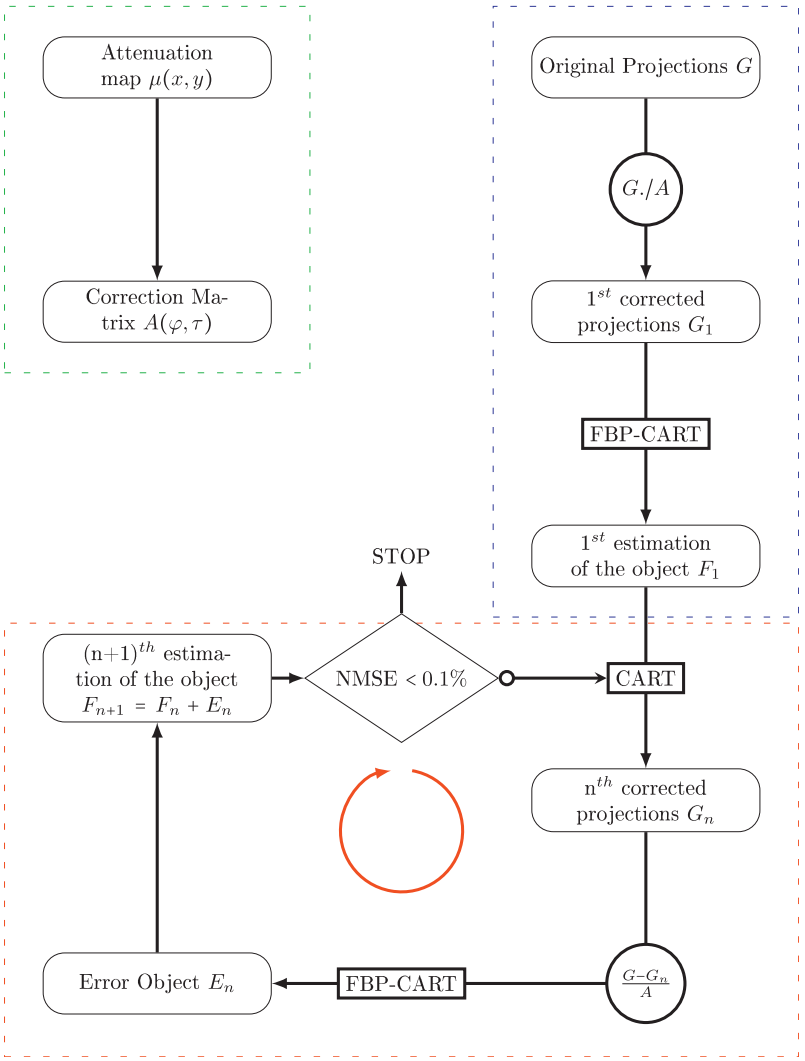

Fig. 20. Principle of the IPC algorithm for the CART.

with p_x is the length of the detection area and I_0 is the source activity. This expression cannot be inverted with the present method. This is why we have to apply an attenuation correction algorithm. We choose the Iterative Pre Correction algorithm (IPC) proposed by Maze [14] and of which the principle is presented by Fig. 20.

First we calculate the forward CART applied on a Shepp-Logan phantom of size 30 cm $\times$ 30 cm (128 $\times$ 128 pixels) with a Monte-Carlo simulation of our CST (Fig. 21). For this simulation we consider a detection length of 1cm and a source activity of 1 MBq. The magnitude of the electron density is 3.34×10^{23} e$^-$/cm^3 and of the attenuation map is 0.157 cm^{-1}. The relative errors obtained between this simulation and the forward CART calculated by Eq. (16) are

$$NMAE = 4.6\% \quad \text{and} \quad NMSE = 0.56\%,$$

which validates the feasibility of our approach as far as data generation is concerned. Then the reconstruction is performed by the IPC-algorithm using the data in Fig. 22. Contours and small structures are well recovered and the relative errors obtained between this reconstructed phantom and the original electron density are

$$NMAE = 3.7\% \quad \text{and} \quad NMSE = 0.08\%,$$

which proves the feasibility of our CST.

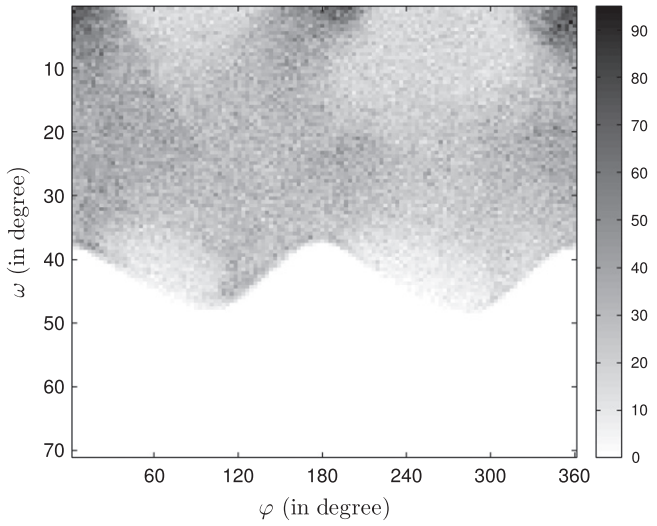

Fig. 21. Monte-Carlo simulation of the CART of the medical phantom shown in Fig. 9.

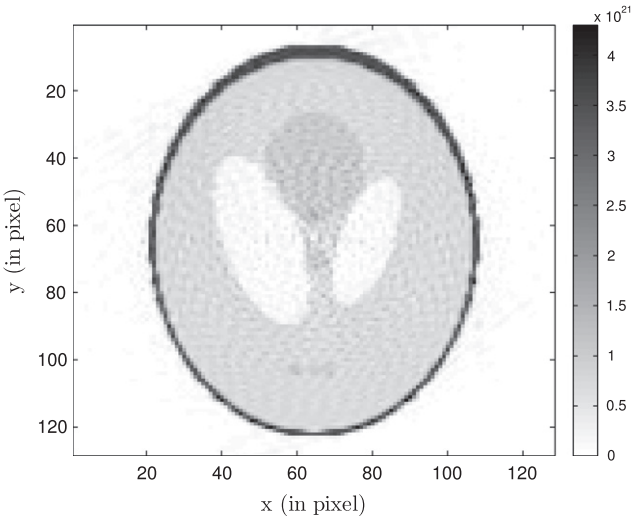

Fig. 22. Reconstruction of the medical phantom shown in Fig. 9 using CART-FBP with attenuation correction and data in Fig. 20.

6. Conclusion and perspectives

A fast algorithm based on the so-called "Filtered Back-Projection" is established in the case of a novel circular-arc Radon transform. This algorithm solves the inversion issue in the case of a new Compton scattering tomography based on CART and simulations prove the feasibility of this new modality. In this new imaging, matter is characterized by its electron density (scattering sites), which has the advantage of being less sensitive to matter aging than its attenuation coefficient used in X-ray tomography. Since this CST modality recovers the electron density of the studied medium whereas the conventional modality recovers the attenuation map, it is hard to compare it. Due to the distribution of the intersections, the CART-FBP gives a reconstruction with more artifacts than the RT-FBP. A sampling theory could be conceived to avoid a too bad distribution of the intersections, and hence increase the quality of the reconstruction, but a linear sampling seems to be sufficient to identify the small structures. It looks like the ordinary Radon transform leads to a good reconstruction quality because it does not include Compton effect in image formation. The CAR transform solves the Compton scattering problem which remains a major technical challenge until now (scattered photons cause blurs, loss of contrast of image and false detections). Moreover the new CST proposes an alternative to the current tomographies keeping at least the same quality of image reconstruction. Transmission Compton tomography can be combined with emission Compton tomography to form a new bimodal

imaging process based on scattered radiation. Modeling and simulation of the last one may be the subject of future investigations.

References

[1] E.M.A. Hussein, D.A. Meneley, S. Banerjee, On the solution of the inverse problem of radiation scattering imaging, Nuclear Science and Engineering 92 (1986) 341–349.
[2] N.V. Arendtsz, E.M.A. Hussein, Energy-spectral compton scatter imaging – part 1: theory and mathematics, IEEE Transactions on Nuclear Sciences 42 (1995) 2155–2165.
[3] R. Guzzardi, G. Licitra, A critical review of compton imaging, CRC Critical Reviews in Biomedical Imaging 15 (1988) 237–268.
[4] M.K. Nguyen, T.T. Truong, On an integral transform and its inverse in nuclear imaging, Inverse Problems 18 (2002) 265–277.
[5] M.K. Nguyen, T.T. Truong, J.L. Delarbre, N. Kitanine, Three dimensional object reconstruction from compton scattered gamma ray data, in: M.S. Ioannis Kakadiaris, J. Kybic (Eds.), Computer Vision and Mathematical Methods in Medical and Bio-medical Image Analysis, 2004, pp. 24–34.
[6] M.K. Nguyen, T.T. Truong, H.D. Bui, J.L. Delarbre, A novel inverse problem in gamma-ray emission imaging, Journal of Inverse Problems in Science and Engineering 12 (2004) 225–246.
[7] J.L. Delarbre, M.K. Nguyen, T.T. Truong, J.L. Starck, Modeling and simulation for scattered gamma-ray imaging, in: Proc. 5th EUROSIM Congress on Modeling and Simulation, Marne la Vallée, France, September 2004.
[8] C. Driol, M.K. Nguyen, T.T. Truong, Modeling and simulation results on high sensitivity scattered gamma-ray imaging, in: Proc. 6th EUROSIM Congress on Modeling and Simulation, Ljubljana, Slovenia, September 2007.
[9] S.J. Norton, Compton scattering tomography, Journal of Applied Physics 76 (1994) 2007–2015.
[10] G. Rigaud, M.K. Nguyen, T.T. Truong, Modeling and simulation results on a new compton scattering tomography, in: EUROSIM (European Simulation and Modeling), Prague, Czech Republic, 2010.
[11] A.K. Louis, Orthogonal function series expansions and the null space of the Radon transform, SIAM Journal on Mathematical Analysis 15 (1984) 621–633.
[12] A.M. Cormack, Radon's problem – old and new, SIAM-AMS Proceedings 14 (1984) 33–39.
[13] M.K. Nguyen, T.T. Truong, Inversion of a new circular-arc radon transform for compton tomography, Inverse Problems 26 (2010) 065005. 13pp.
[14] A. Maze, J.L. Cloirec, R. Collorec, Y. Bizais, P. Briandet, P. Bourguet, Iterative reconstruction methods for nonuniform attenuation distribution in SPECT, Journal of Nuclear Medicine 34 (1993) 1204–1209.